


SCIENTIFIC REPORTS



OPEN

Thermal Conductivity of Graphene-hBN Superlattice Ribbons

Isaac M. Felix & Luiz Felipe C. Pereira 

Superlattices are ideal model systems for the realization and understanding of coherent (wave-like) and incoherent (particle-like) phonon thermal transport. Single layer heterostructures of graphene and hexagonal boron nitride have been produced recently with sharp edges and controlled domain sizes. In this study we employ nonequilibrium molecular dynamics simulations to investigate the thermal conductivity of superlattice nanoribbons with equal-sized domains of graphene and hexagonal boron nitride. We analyze the dependence of the conductivity with the domain sizes, and with the total length of the ribbons. We determine that the thermal conductivity reaches a minimum value of $89 \text{ W m}^{-1}\text{K}^{-1}$ for ribbons with a superlattice period of 3.43 nm. The effective phonon mean free path is also determined and shows a minimum value of 32 nm for the same superlattice period. Our results also reveal that a crossover from coherent to incoherent phonon transport is present at room temperature for BNC nanoribbons, as the superlattice period becomes comparable to the phonon coherence length. Analyzing phonon populations relative to the smallest superlattice period, we attribute the minimum thermal conductivity to a reduction in the population of flexural phonons when the superlattice period equals 3.43 nm. The ability to manipulate thermal conductivity using superlattice-based two-dimensional materials, such as graphene-hBN nanoribbons, opens up opportunities for application in future nanostructured thermoelectric devices.

Over the past few decades, heat transport in high-performance nanostructured thermoelectric materials has been controlled primarily by the introduction of atomic-scale impurities, interfaces and defects^{1–6}. Such structural changes reduce heat flow by scattering phonons diffusely. A recent approach used for controlling nanoscale heat transport involves phonon wave interference effects, such as the one due to specular reflection and transmission of thermal vibrations at interfaces^{7–9}. Superlattices are excellent candidates for this approach because of their atomically flat interfaces, since wave-interference effects depend on the interface conditions. Smoother interfaces lead to greater wave interference effects whereas very rough interfaces scatter phonons diffusely. That is to say, high-quality interfaces favor specular reflection and transmission of phonons^{8–10}.

A superlattice corresponds to a periodic or quasi-periodic arrangement of different materials, and can be described by a superlattice period which confers a new translational symmetry to the system, impacting their phonon dispersions and subsequently their thermal transport properties¹¹. Superlattices are ideal model systems for the realization and understanding of both coherent (wave-like) and incoherent (particle-like) phonon transport. Coherent phonons are subject to wave interference whereas incoherent phonons are subject to diffuse scattering. A prime example has been experimentally demonstrated in GaAs/AlAs superlattices, where the phase of coherent phonons is preserved across interfaces and they can travel ballistically over long distances⁷. Similarly, it has been experimentally verified in epitaxial perovskite oxide superlattices that there is a crossover from coherent to incoherent phonon transport, which manifests itself as a minimum in lattice thermal conductivity as a function of interface density⁸. In spite of the recent advances, the idea of using periodic structures such as superlattices to control thermal transport by manipulating coherent phonons has been around for a few decades¹². The existence of a minimum thermal conductivity for a given superlattice period, due to the competition between particle and wave nature of phonons in epitaxial perovskite oxide superlattices is one of the most important and long-standing predictions regarding thermal transport in superlattices^{10,13}.

Graphene shows weak Umklapp scattering due to its two-dimensional phonon dispersion relation^{14,15}. This feature makes graphene attractive for studying coherent phonon transport in nanostructures, such as graphene-hexagonal boron nitride monolayer superlattices (BNC superlattices). The lattice parameter of the honeycomb structures of graphene and hexagonal boron nitride monolayer (hBN) are nearly the same, enabling

Departamento de Física, Universidade Federal do Rio Grande do Norte, Natal, 59078-970, Brazil. Correspondence and requests for materials should be addressed to I.M.F. (email: felix@fisica.ufrn.br) or L.F.C.P. (email: pereira@fisica.ufrn.br)

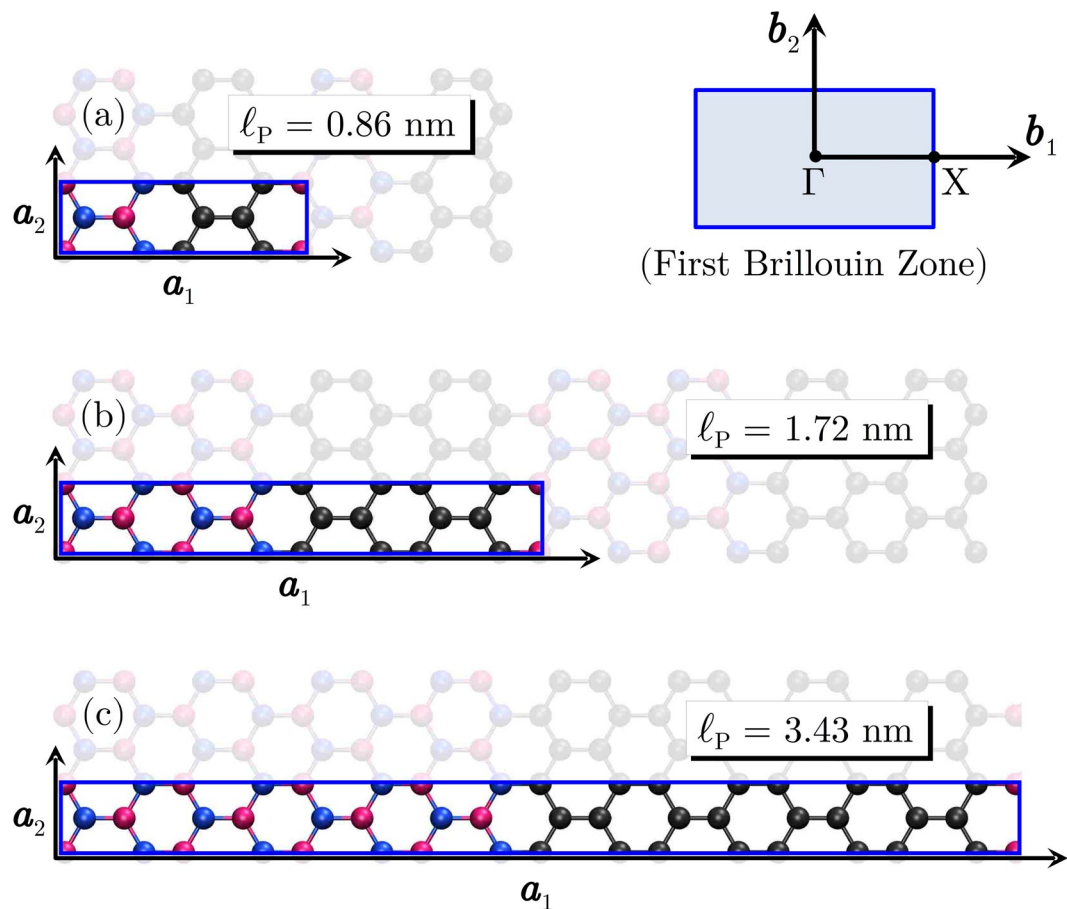


Figure 1. Unit cell of graphene-hBN structures with increasing superlattice period ℓ_P . All ribbons have nominal width of 5 nm and thickness of 0.33 nm. Gray spheres represent carbon atoms, pink spheres are boron atoms and blue spheres are nitrogen atoms. First Brillouin zone and corresponding high-symmetry points are also shown in the top-right panel.

the synthesis of superlattices with smooth interfaces¹⁶, which favors specular scattering of phonons, as discussed above. Graphene is a semi-metal¹⁷ whereas hBN could be seen as its insulating counterpart^{18,19}. Concerning their thermal transport properties, graphene presents the highest thermal conductivity among known materials^{20–23}, while hBN's thermal conductivity is one order of magnitude smaller, but still larger than many bulk semiconductors^{19,24}. In both graphene and hBN, at room temperature, phonons are the main heat carriers.

Recently, uniform monolayer graphene-hBN structures have been successfully synthesized via lithography patterning coupled with chemical vapor deposition (CVD)^{16,25–27}. It was observed that the formation of BNC structures with zigzag interfaces was preferred over that with armchair interfaces during growth²⁷. This approach enables fabrication of large-scale hybrid graphene-hBN heterostructures that are continuous and easily transferable to substrates¹⁶. It has also been shown that these materials possess unusual physical properties, different from pristine graphene and h-BN^{25,28–34}. For instance, both theoretical analysis and experimental results show that the band gap of BNC could be tuned by arranging graphene and hBN domains in various ways^{25,28–30}. It has been reported that graphene embedded in hBN with zigzag interfaces always originates semiconducting structures²⁹. It was also reported that the Seebeck coefficient of BNC superlattices can be 20 times larger than that of graphene, and that it is highly sensitive to the proportion of hBN in the lattice^{35,36}. It has also been found that the thermal conductivity of graphene embedded in hBN depends on hBN concentration and cluster size^{37–39}. There are other examples of how the chemical and structural diversities in BNC monolayers affect their thermal transport properties^{37–40}.

In this work we investigate the heat transport properties of BNC superlattice ribbons with fixed width and equal-sized domains of graphene and hBN, as shown in Fig. 1, via non-equilibrium molecular dynamics simulations. We have considered only zigzag-oriented graphene-hBN interfaces, since those are preferred during growth²⁷, but we do not expect our main results to depend on the interface orientation. We analyze the dependence of the conductivity with the domain sizes, and with the total length of the ribbons. We observe a non-monotonic behavior of the conductivity with the superlattice period and identify the corresponding value for which the thermal conductivity is a minimum. Considering the dependence of the conductivity with the length of the ribbons, we determine an effective phonon mean free path (MFP), which also has a minimum value for the same superlattice period.

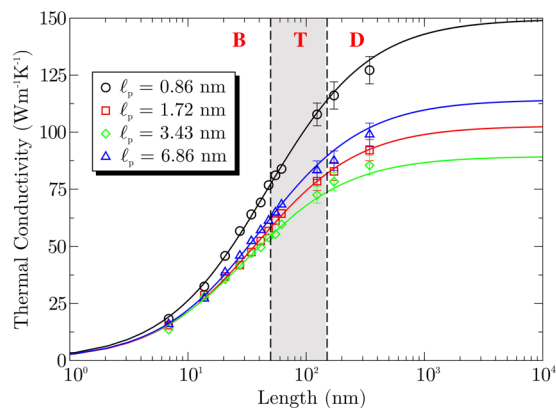


Figure 2. Thermal conductivity as a function of length for increasing superlattice period ℓ_p . The dashed lines indicate the ballistic transport regime (B), the diffusive regime (D), and the ballistic-diffusive transition (T). Lines are fit to Eq. (1), excluding the three largest systems, which shows its predictive power. We only show error bars for larger system sizes, for all others the uncertainties are smaller than symbol sizes.

Results

Thermal conductivity dependence with sample length. Due to strong size effects arising from the limitation of the phonon MFP to the region between the heat reservoirs, the conductivity for a system of length L_x is expected to behave as:⁴¹

$$\frac{1}{\kappa(L_x)} = \frac{1}{\kappa_\infty} \left(1 + \frac{\Lambda_{\text{ph}}}{L_x} \right), \quad (1)$$

where κ_∞ is the intrinsic (length-independent) conductivity of the material, and Λ_{ph} is the effective MFP of the heat carriers. Therefore, by fitting the above expression to the simulation data obtained for systems of increasing length we can calculate both, the intrinsic thermal conductivity of the material as well as its effective MFP. In our case, the thermal conductivity is expected to depend on the ribbon length L_x as described in Eq. (1), but also on the superlattice period ℓ_p . From this dependence we can extract the intrinsic thermal conductivity and the effective phonon MFP for each superlattice period. Figure 2 shows the length dependence of κ for four superlattice periods, starting from the smallest period considered, 0.86 nm and up to 6.86 nm. For each superlattice period we observe an increase in conductivity with ribbon length, which is described by Eq. (1) represented by the continuous lines in Fig. 2. The fitting was performed without the three longest systems, which were obtained later and present larger uncertainties, but agree with the fitted lines within the error bars. In fact, including the three longer systems in the fitting of Eq. (1), the intrinsic thermal conductivity κ_∞ would change by less than 5%. This agreement shows the remarkable predictive power of Eq. (1), which can be used to predict the intrinsic lattice thermal conductivity from simulations with relatively short systems^{42–44}.

Analyzing the behavior of $\kappa(L_x)$ we observe three heat transport regimes, as indicated in Fig. 2. First the ballistic regime where $\kappa \propto L_x$, which is valid in the small L_x region B, up to ≈ 50 nm. In this region the phonon MFP is larger than the system length, and is thus limited by it. For $L_x > 150$ nm, we observe the diffusive regime where κ shows a weak dependence on system length. Here the phonon MFP is shorter than the system length. Finally, between these two regions we find a ballistic-diffusive transition regime, region T, where the system length becomes comparable to the phonon MFP and the dependence of κ on L_x decreases.

Thermal conductivity and effective phonon MFP as a function of superlattice period. In Fig. 3(a) we present the intrinsic thermal conductivity κ_∞ of the BNC nanoribbons as a function of superlattice period ℓ_p at 300 K. We observe that the overall superlattice thermal conductivities are remarkably reduced, by $\sim 98\%$ when compared with the thermal conductivity of graphene^{20,22,23}, and by $\sim 78\%$ when compared with the thermal conductivity of hBN^{24,45}. Another noticeable feature in Fig. 3(a) is the non-monotonic dependence of κ_∞ on ℓ_p . An increase in ℓ_p initially causes κ_∞ to decrease until it reaches a minimum value of $89 \text{ W m}^{-1}\text{K}^{-1}$ when $\ell_p = 3.43$ nm, and then it increases. Our results are in general agreement with previous reports which investigated the influence of the superlattice period on the thermal conductivity of BNC superlattices. The observation of a minimum thermal conductivity for a specific superlattice period, as found in our simulations, has been reported by Jiang *et al.*⁴⁶, Zhu and Ertekin⁴⁷, da Silva *et al.*⁴⁸, and Chen *et al.*⁴⁹. However, in our work there are two factors not considered in previous works. First, we deal with nanoribbons rather than 2D superlattices, as done in the previous works^{46–49}. Therefore, our systems are expected to present more of a 1D character than a 2D one. Second, we consider the intrinsic thermal conductivity of the BNC nanoribbons by employing Eq. (1), while previous works have reported length-dependent conductivities^{46–49}. Our numerical estimate for the superlattice period which yields the minimum thermal conductivity is in excellent agreement with the one reported by Chen *et al.*⁴⁹, although their minimum conductivity is approximately twice as much as ours, which can be explained by the fixed system length they used or due to the different width of their supercell.

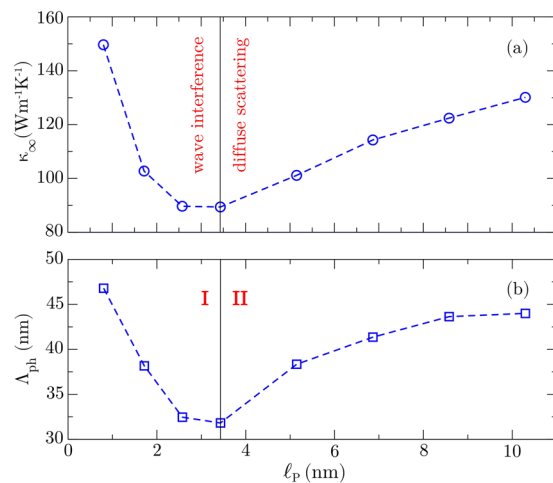


Figure 3. (a) Intrinsic thermal conductivity and (b) effective phonon mean free path as a function of superlattice period. Both quantities reach a minimum value at $\ell_p = 3.43$ nm, which marks the interface between coherent and incoherent phonon transport. The dashed lines are just a guide to the eye.

In general, the minimum thermal conductivity is a consequence of a crossover from coherent to incoherent phonon transport. To the left of the minimum, Brillouin zone folding occurs due to the phonon wave effect, which explains the reduction of thermal conductivity when increasing ℓ_p ⁴⁹. To the right of the minimum, the number of interfaces (or thermal resistors) decreases with ℓ_p , thus easing heat conduction^{50–53}. Indeed, it has been shown that thermal conductivity decreases when the structure periodicity is dominated by wave interference effects and increases when it depends on diffuse interface scattering¹⁰. This can also be understood considering that, in general, low-frequency phonons are more likely to experience wave interference effects, such as specular reflection and transmission, due to their large wavelengths, whereas high-frequency phonons are likely to be scattered diffusely at the interfaces^{9,10}. Thus, the combination of wave interference effects and diffuse interface scattering leads to a local minimum of thermal conductivity as a function of superlattice period.

Nonetheless, for phonons experiencing wave interference, the thermal conductivity decreases with superlattice period due to the modification of the bulk phonon dispersion relation. This is caused by zone folding and band flattening, which reduce phonon group velocities as the lattice period increases, thereby decreasing the thermal conductivity⁵⁴. Therefore, we can say that, the combination of wave interference effects and diffuse interface scattering leads to a local minimum of thermal conductivity as a function of superlattice period¹⁰. Note that, for region II in Fig. 3, κ rises with increasing period, an indicator that the thermal energy is carried primarily by particle-like phonons (incoherent) that are scattered diffusely at the interfaces. On the other hand, for region I, κ decreases with increasing period. This behavior is not compatible with the presence of diffuse scattering only, and one can assume that part of the heat is carried by wave-like phonons (coherent) experiencing interference effects. Thus, the observation of a minimum thermal conductivity as a function of superlattice period presents direct evidence of the crossover from coherent to incoherent phonon transport in these superlattices. Our results reveal that wave interference for thermal phonons and the crossover from coherent to incoherent phonon transport can be present at room temperature for BNC nanoribbons. Similar behavior has been observed in experiments with epitaxial perovskite oxide superlattices⁸.

The lowest thermal conductivity is observed when ℓ_p is comparable to the phonon coherence length in the superlattice^{11,47}. This critical length can be much smaller than the effective phonon MFP of the superlattices. In our simulations, the smallest thermal conductivity $\kappa_\infty = 89 \text{ W m}^{-1}\text{K}^{-1}$ was found for a superlattice with $\ell_p = 3.43$ nm. Thus, this corresponds to the coherence length of phonons in graphene-hBN superlattice ribbons, in agreement with the predictions by Zhu and Ertekin⁴⁷. From the data in Fig. 3(b) we estimate Λ_{ph} in a superlattice with $\ell_p = 3.43$ nm to be 32 nm. This value is one order of magnitude larger than the coherence length, also in agreement with Zhu and Ertekin⁴⁷. Notice that phonons experience ballistic transport for system lengths shorter than Λ_{ph} , which can reach distances much larger than the coherence length, in agreement with the increasing trend in thermal conductivities shown in Fig. 2.

Phonon dispersions. In order to better understand the dependence of the thermal conductivity on the superlattice period we have investigated the phonon dispersion for several periods. The phonon dispersion relations were calculated with the General Utility Lattice Program (GULP), which implements lattice dynamics methods⁵⁵. The interatomic potential used was the same as in the MD simulations. Figure 1 illustrates the unit cells with superlattice periods of 0.86 nm, 1.72 nm and 3.43 nm. It also shows the first Brillouin zone of the structures, along with its high-symmetry points. For $\ell_p = 0.86$ nm, the unit cell is composed of 8 non-equivalent atoms, 4 carbon atoms (gray spheres), 2 boron atoms (pink spheres) and 2 nitrogen atoms (blue spheres). In Fig. 1 we also illustrate the first Brillouin zone for our unit cell, with high-symmetry points $\Gamma = (0, 0, 0)$, $X = (\frac{1}{2}, 0, 0)$, in units of reciprocal lattice vectors.

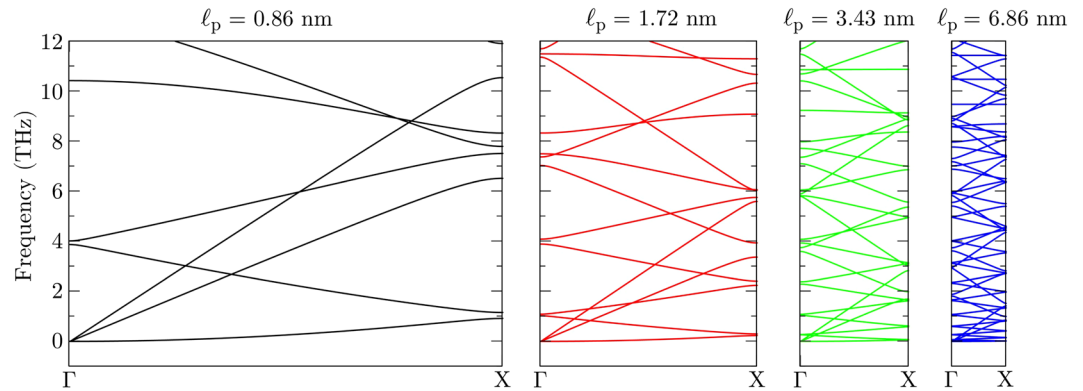


Figure 4. Phonon dispersion for superlattices of increasing period. Only the region around the acoustic phonon modes is shown.

In Fig. 4 we present phonon dispersions for increasing superlattice periods. Only the frequency range covered by the acoustic modes is shown, since those are the main heat carriers. It is important to remember that the number of non-equivalent atoms in the unit cell is proportional to the period, so that the number of vibrational modes follows the same trend. There is a reduction of phonon group velocities (slope of the dispersion curves) with increasing superlattice period due to zone folding. This explains the reduction of thermal conductivity in region I of Fig. 3, where coherent phonons dominate thermal transport and where there must be a superposition of Bloch waves^{10,56}. However, this analysis cannot elucidate what happens in region II of Fig. 3, where diffuse scattering dominates, because boundaries scatter phonons diffusely. It is commonly assumed that such scattering processes randomizes the phonon phases such that interference effects, and the resultant modification of the phonon dispersion, can be neglected⁷.

Vibrational spectrum and period-induced changes in phonon populations. In order to understand the physical origins of the minimum thermal conductivity for a specific superlattice period, we analyze the vibrational spectrum of BNC superlattices. First, we calculated the velocity autocorrelation function (VACF) by post processing 100 ps trajectories, in which atomic velocities are printed out every 5 fs. The VACF is then normalized such that $\text{VACF}(t = 0) = 1$, and averaged over all atoms in the supercell. The vibrational density of states (VDOS) is then calculated from the Fourier transform of the averaged VACF

$$\text{VDOS}(\omega) = \int_0^\infty \frac{\langle v(0) \cdot v(t) \rangle}{\langle v(0) \cdot v(0) \rangle} e^{-i\omega t} dt, \quad (2)$$

where v is the atomic velocity, $\langle v(0) \cdot v(t) \rangle$ is the VACF and ω is the angular frequency.

In Fig. 5(a) we present the total VDOS for each ℓ_p . The number of pronounced peaks decreases as the superlattice period increases, which is due to the increase in size of the unit cell. In general, pronounced peaks in the phonon spectra indicate the presence of coherent phonons. Therefore, as ℓ_p increases, fewer coherent phonons should be present in the superlattice. For two-dimensional materials, the flexural modes ZA/ZO are the major contributors in thermal transport, while longitudinal LA/LO and transverse TA/TO modes play a smaller role^{21,23,57–59}.

Figure 5(b–e) show the changes in phonon populations due to an increase in superlattice period, relative to $\ell_p = 0.86$ nm, which are calculated from the ratio between the occupation of phonon modes, defined as

$$\Delta n(\omega) = \frac{1 + \int_0^\omega \text{VDOS}_{\ell_p} d\omega'}{1 + \int_0^\omega \text{VDOS}_{\ell_p=0.86\text{nm}} d\omega'} - 1. \quad (3)$$

Therefore, $\Delta n(\omega) = 0$ corresponds to no change in occupation, $\Delta n(\omega) < 0$ indicates a decrease in population and $\Delta n(\omega) > 0$ to an increase relative to $\ell_p = 0.86$ nm. Notice that for $\ell_p = 1.72$ nm the total occupation of phonon modes shows no major alterations up to frequencies around 4 THz, while there is a clear decrease in phonon populations in the low-frequency region for superlattice periods $\ell_p = 3.43$ nm and $\ell_p = 6.86$ nm. Furthermore, our data shows that the largest decrease in populations happens for $\ell_p = 3.43$ nm, which is the superlattice period for the structures with the lowest conductivity. Analyzing the changes in populations for each polarization branch, we notice a small increase of LA/LO and TA/TO modes up to frequencies of 20 THz. In panel (e) we notice a pronounced decrease in phonon populations for ZA/ZO modes, and that the largest decrease below 10 THz happens for $\ell_p = 3.43$ nm. Therefore, we can attribute the minimum thermal conductivity observed for BNC superlattices with a period of 3.43 nm to the reduction in population of flexural phonons for that period. This behavior has not been considered in any of the previous works dealing with BNC superlattices.

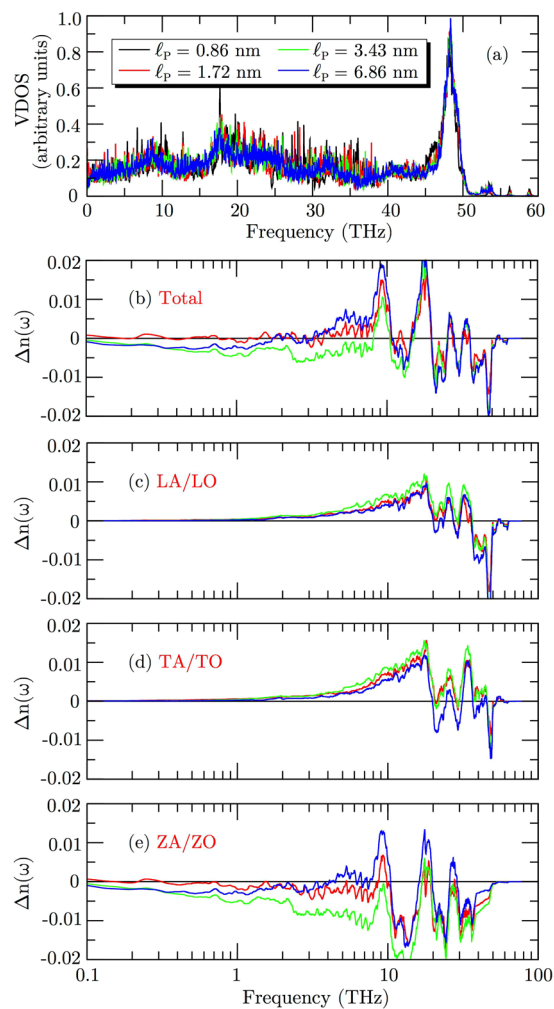


Figure 5. (a) Vibrational density of states for BNC superlattices. (b–e) Changes in phonon populations due to superlattice period increase relative to $\ell_p = 0.86$ nm.

Discussion

From our interpretation of the physical origins of the conductivity reduction in BNC superlattices, we can construct a pictorial representation of phonon scattering at the interfaces between graphene and hBN, which is shown in Fig. 6. For $\ell_p < 3.43$ nm, the wavelength of heat carrying phonons is larger than the individual domains, so they suffer small influence of the interfaces, and transport is coherent. For $\ell_p > 3.43$ nm, the wavelength of heat carrying phonons is smaller than the individual domains, and they experience a larger influence of the interfaces, therefore transport is incoherent. In the case of $\ell_p = 3.43$ nm the wavelength of heat carrying phonons is comparable to the size of individual domains, and we have a transition from the coherent to the incoherent transport regimes, which is responsible for the minimum thermal conductivity observed for this superlattice period.

Finally, it is important to comment on the possible experimental realization of these BNC superlattice ribbons. Our results should be seen as an upper bound for the conductivities that could be measured in experiments, since we consider perfect superlattices, with perfect edges and interfaces, and in the absence of isotopic disorder. Any experimental realization of these superlattices is bound to present some of these defects, which are known to reduce heat transport. Another limitation is related to the superlattice period which yields the minimum conductivity. Producing a BNC superlattice with a period smaller than 5 nm could be challenging. Therefore, it is possible that the experiments would not observe the minimum value of κ_∞ but only the weakly increasing trend observed in region II of Fig. 3.

Methods

Molecular dynamics (MD) simulations in the present work were performed with LAMMPS (Large-scale Atomic/Molecular Massively Parallel Simulator)⁶⁰. We employed the Tersoff empirical potential recently re-parametrized to accurately reproduce the vibrational properties of carbon and hBN nanostructures^{39,61,62}. The thermal conductivity of BNC nanoribbons was calculated via non-equilibrium molecular dynamics (NEMD) simulations with periodic boundary conditions along the heat current direction, and free boundary conditions in the other directions. In all simulations the equations of motion were integrated with a 0.5 fs timestep. The systems were initially

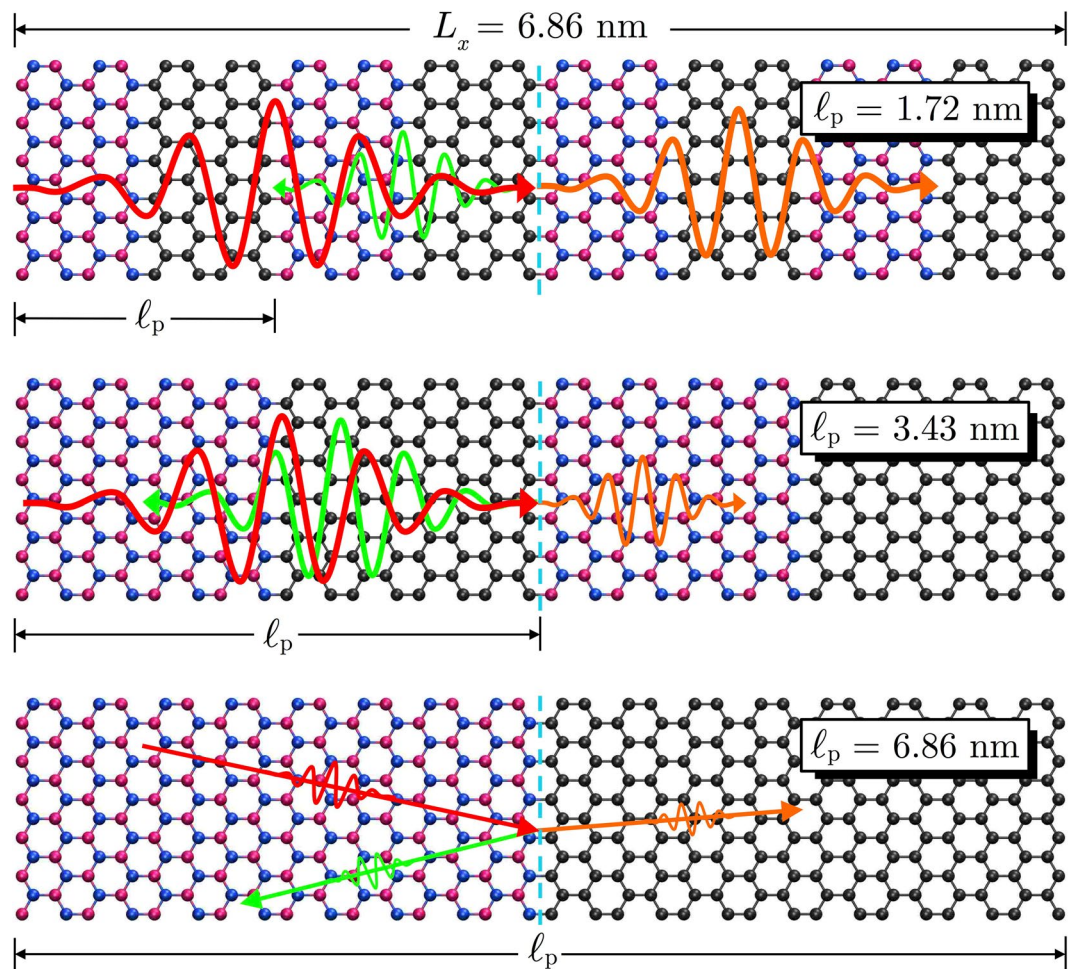


Figure 6. Representative scheme of both coherent (wave interference) and incoherent (diffuse scattering) phonon transport.

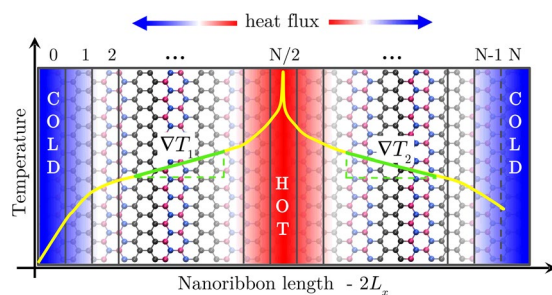


Figure 7. Set-up for the reverse NEMD method. A heat flux is imposed by exchanging the kinetic energy of slow particles in the hot region with fast particles in the cold region. The image of the cold layer becomes the N -th layer, such that layers 0 and N are the same. Also shown is the temperature profile from which the temperature gradient is calculated.

thermalized with a Nosé-Hoover thermostat at 300 K for 100 ps. Each ribbon was relaxed at finite temperature in order to achieve zero-stress along the periodic direction, the stress along the other two directions is zero on average. The thermostat was turned off once the system reached equilibrium, such that the equations of motion were then integrated under microcanonical conditions.

We employed the so-called reverse NEMD method, proposed by Müller-Plathe, to impose a heat flux in the system⁶⁵. The heat flux is imposed by exchanging the kinetic energy of slow moving particles in the “hot” region with fast moving particles in the “cold” region, as shown in Fig. 7. The cold region is at the left end of the simulation box, while the hot region is at its center. Due to periodic boundary conditions, the image of the cold region becomes the N -th layer, such that regions 0 and N are the same. On average each region had 100–200 atoms in

total. The kinetic energy swaps were performed every 1000 timesteps. The heat flux is obtained from the difference in kinetic energy of the exchanged particles as

$$J(t) = \frac{1}{2tA} \sum_{\text{exchanges}} \frac{m_i v_i^2 - m_j v_j^2}{2}, \quad (4)$$

where A is the cross sectional area of the sheet which we define as the width of the ribbon multiplied by its thickness. All ribbons have nominal width of 5 nm (in y -direction) and we assume a thickness of 0.33 nm for graphene and hBN (in z -direction).

After a transient time interval the stationary regime is achieved, where the heat flux reaches a constant average value. In most simulations the stationary regime is established after 20 ns, corresponding to 40×10^6 simulation steps. With the system in its stationary regime, we divide it in several slabs along the direction of the heat flux and calculate the temperature in each slab from the average kinetic energy of the particles within the slab, according to the equipartition theorem, as:

$$T_i = \frac{2}{3n_i k_B} \sum_j \frac{p_j^2}{2m_j}, \quad (5)$$

where T_i is the temperature of i -th slab, n_i is the number of atoms in i -th slab, k_B is Boltzmann's constant, m_j and p_j are atomic mass and momentum of atom j , respectively. Thus, the temperature gradient is calculated from the average temperature in each region of the system.

Once the heat flux and the temperature gradient are stationary we obtain the thermal conductivity for a sample of size L_x directly from Fourier law

$$\kappa(L_x) = \frac{\langle J_x \rangle}{\nabla_x T}, \quad (6)$$

where $\nabla_x T$ is the arithmetic mean of the temperature gradient considering both directions of heat transport (as shown in Fig. 7)

$$\nabla_x T = \frac{|\nabla_x T_1| + |\nabla_x T_2|}{2}. \quad (7)$$

Data availability. The datasets generated and analyzed during the current study are available from the corresponding author on reasonable request.

References

- Kim, W., Wang, R. & Majumdar, A. Nanostructuring expands thermal limits. *Nano Today* **2**, 40 (2007).
- Snyder, G. J. & Toberer, E. S. Complex thermoelectric materials. *Nat. Mater.* **7**, 105 (2008).
- Poudel, B. *et al.* High-thermoelectric performance of nanostructured bismuth antimony telluride bulk alloys. *Science* **320**, 634 (2008).
- Li, X., Maute, K., Dunn, M. L. & Yang, R. Strain effects on the thermal conductivity of nanostructures. *Phys. Rev. B* **81**, 245318 (2010).
- Vaqueiro, P. & Powell, A. V. Recent developments in nanostructured materials for high-performance thermoelectrics. *J. Mater. Chem.* **20**, 9577 (2010).
- Toberer, E. S., Baranowski, L. L. & Dames, C. Advances in thermal conductivity. *Annu. Rev. Mater. Res.* **42**, 179 (2012).
- Luckyanova, M. N. *et al.* Coherent phonon heat conduction in superlattices. *Science* **338**, 936 (2012).
- Ravichandran, J. *et al.* Crossover from incoherent to coherent phonon scattering in epitaxial oxide superlattices. *Nat. Mater.* **13**, 168 (2014).
- Maldovan, M. Phonon wave interference and thermal bandgap materials. *Nat. Mater.* **14**, 667 (2015).
- Simkin, M. V. & Mahan, G. D. Minimum thermal conductivity of superlattices. *Phys. Rev. Lett.* **84**, 927 (2000).
- Latour, B., Volz, S. & Chalopin, Y. Microscopic description of thermal-phonon coherence: From coherent transport to diffuse interface scattering in superlattices. *Phys. Rev. B* **90**, 014307 (2014).
- Narayanaamurti, V. Phonon optics and phonon propagation in semiconductors. *Science* **213**, 717 (1981).
- Chen, Y., Li, D., Lukes, J. R., Ni, Z. & Chen, M. Minimum superlattice thermal conductivity from molecular dynamics. *Phys. Rev. B* **72**, 174302 (2005).
- Nika, D., Pokatilov, E., Askerov, A. & Balandin, A. A. Phonon thermal conduction in graphene: Role of Umklapp and edge roughness scattering. *Phys. Rev. B* **79**, 155413 (2009).
- Lindsay, L., Broido, D. & Mingo, N. Flexural phonons and thermal transport in graphene. *Phys. Rev. B* **82**, 115427 (2010).
- Liu, Z. *et al.* In-plane heterostructures of graphene and hexagonal boron nitride with controlled domain sizes. *Nat. Nanotechnol.* **8**, 119 (2013).
- Novoselov, K. S. *et al.* Electric field effect in atomically thin carbon films. *Science* **306**, 666 (2004).
- Nagashima, A., Tejima, N., Gamou, Y., Kawai, T. & Oshima, C. Electronic structure of monolayer hexagonal boron nitride physisorbed on metal surfaces. *Phys. Rev. Lett.* **75**, 3918 (1995).
- Watanabe, K., Taniguchi, T. & Kanda, H. Direct-bandgap properties and evidence for ultraviolet lasing of hexagonal boron nitride single crystal. *Nat. Mater.* **3**, 404 (2004).
- Balandin, A. A. *et al.* Superior thermal conductivity of single-layer graphene. *Nano Lett.* **8**, 902 (2008).
- Seol, J. H. *et al.* Two-dimensional phonon transport in supported graphene. *Science* **328**, 213 (2010).
- Xu, X. *et al.* Length-dependent thermal conductivity in suspended single-layer graphene. *Nat. Commun.* **5**, 3689 (2014).
- Fan, Z. *et al.* Thermal conductivity decomposition in two-dimensional materials: Application to graphene. *Phys. Rev. B* **95**, 144309 (2017).
- Mortazavi, B., Pereira, L. F. C., Jiang, J.-W. & Rabczuk, T. Modelling heat conduction in polycrystalline hexagonal boron-nitride films. *Sci. Rep.* **5**, 13228 (2015).
- Ci, L. *et al.* Atomic layers of hybridized boron nitride and graphene domains. *Nat. Mater.* **9**, 430 (2010).

26. Levendorf, M. P. *et al.* Graphene and boron nitride lateral heterostructures for atomically thin circuitry. *Nature* **488**, 627 (2012).
27. Gao, Y. *et al.* Toward single-layer uniform hexagonal boron nitride–graphene patchworks with zigzag linking edges. *Nano Lett.* **13**, 3439 (2013).
28. Ding, Y., Wang, Y. & Ni, J. Electronic properties of graphene nanoribbons embedded in boron nitride sheets. *Appl. Phys. Lett.* **95**, 123105 (2009).
29. Seol, G. & Guo, J. Bandgap opening in boron nitride confined armchair graphene nanoribbon. *Appl. Phys. Lett.* **98**, 143107 (2011).
30. Shinde, P. P. & Kumar, V. Direct band gap opening in graphene by BN doping: Ab initio calculations. *Phys. Rev. B* **84**, 125401 (2011).
31. Kan, M., Zhou, J., Wang, Q., Sun, Q. & Jena, P. Tuning the band gap and magnetic properties of BN sheets impregnated with graphene flakes. *Phys. Rev. B* **84**, 205412 (2011).
32. Bernardi, M., Palummo, M. & Grossman, J. C. Optoelectronic properties in monolayers of hybridized graphene and hexagonal boron nitride. *Phys. Rev. Lett.* **108**, 226805 (2012).
33. Jain, N., Bansal, T., Durcan, C. A., Xu, Y. & Yu, B. Monolayer graphene/hexagonal boron nitride heterostructure. *Carbon* **54**, 396 (2013).
34. Zhou, H. *et al.* High thermal conductivity of suspended few-layer hexagonal boron nitride sheets. *Nano Res.* **7**, 1232 (2014).
35. Yang, N. & Ni, X. Jiang, J.-w. & Li, B. How does folding modulate thermal conductivity of graphene? *Appl. Phys. Lett.* **100**, 093107 (2012).
36. Yokomizo, Y. & Nakamura, J. Giant seebeck coefficient of the graphene/h-BN superlattices. *Appl. Phys. Lett.* **103**, 113901 (2013).
37. Jiang, J.-W., Wang, B.-S. & Wang, J.-S. First principle study of the thermal conductance in graphene nanoribbon with vacancy and substitutional silicon defects. *Appl. Phys. Lett.* **98**, 113114 (2011).
38. Sevincli, H., Li, W., Mingo, N., Cuniberti, G. & Roche, S. Effects of domains in phonon conduction through hybrid boron nitride and graphene sheets. *Phys. Rev. B* **84**, 205444 (2011).
39. Kinaci, A., Haskins, J. B., Sevik, C. & Cagin, T. Thermal conductivity of BN-C nanostructures. *Phys. Rev. B* **86**, 115410 (2012).
40. Song, J. & Medhekar, N. V. Thermal transport in lattice-constrained 2D hybrid graphene heterostructures. *J. Phys. Condens. Matter* **25**, 445007 (2013).
41. Schelling, P. K., Phillpot, S. R. & Keblinski, P. Comparison of atomic-level simulation methods for computing thermal conductivity. *Phys. Rev. B* **65**, 144306 (2002).
42. Pereira, L. F. C., Mortazavi, B., Makaremi, M. & Rabczuk T. Anisotropic thermal conductivity and mechanical properties of phagraphene: A molecular dynamics study. *RSC Adv.* **6**, 57773 (2016).
43. Mortazavi, B., Rahaman, O., Rabczuk, T. & Pereira, L. F. C. Thermal conductivity and mechanical properties of nitrogenated holey graphene. *Carbon* **106**, 1 (2016).
44. Mortazavi, B., Le, M.-Q., Rabczuk, T. & Pereira, L. F. C. Anomalous strain effect on the thermal conductivity of borophene: A reactive molecular dynamics study. *Phys. E Low-dimensional Syst. Nanostruct.* **93**, 202 (2017).
45. Sevik, C., Sevincli, H., Cuniberti, G. & Cagin, T. Phonon engineering in carbon nanotubes by controlling defect concentration. *Nano Lett.* **11**, 4971 (2011).
46. Jiang, J.-W. W., Wang, J.-S. S. & Wang, B.-S. S. Minimum thermal conductance in graphene and boron nitride superlattice. *Appl. Phys. Lett.* **99**, 97 (2011).
47. Zhu, T. & Ertekin, E. Phonon transport on two-dimensional graphene/boron nitride superlattices. *Phys. Rev. B* **90**, 195209 (2014).
48. Da Silva, C., Saiz, F., Romero, D. A. & Amon, C. H. Coherent phonon transport in short-period two-dimensional superlattices of graphene and boron nitride. *Phys. Rev. B* **93**, 125427 (2016).
49. Chen, X.-K., Xie, Z.-X., Zhou, W.-X., Tang, L.-M. & Chen, K.-Q. Phonon wave interference in graphene and boron nitride superlattice. *Appl. Phys. Lett.* **109**, 023101 (2016).
50. Yao, T. Thermal properties of AlAs/GaAs superlattices. *Appl. Phys. Lett.* **51**, 1798 (1987).
51. Swartz, E. T. & Pohl, R. O. Thermal boundary resistance. *Rev. Mod. Phys.* **61**, 605 (1989).
52. Lee, S.-M., Cahill, D. G. & Venkatasubramanian, R. Thermal conductivity of Si-Ge superlattices. *Appl. Phys. Lett.* **70**, 2957 (1997).
53. Dames, C. & Chen, G. Theoretical phonon thermal conductivity of Si/Ge superlattice nanowires. *J. Appl. Phys.* **95**, 682 (2004).
54. Tamura, S.-i., Tanaka, Y. & Maris, H. Phonon group velocity and thermal conduction in superlattices. *Phys. Rev. B* **60**, 2627 (1999).
55. Gale, J. D. & Rohl, A. L. The General Utility Lattice Program (GULP). *Mol. Simul.* **29**, 291 (2003).
56. Tamura, S., Hurley, D. C. & Wolfe, J. P. Acoustic-phonon propagation in superlattices. *Phys. Rev. B* **38**, 1427 (1988).
57. Prasher, R. Graphene spreads the heat. *Science* **328**, 185 (2010).
58. Zhang, H., Lee, G. & Cho, K. Thermal transport in graphene and effects of vacancy defects. *Phys. Rev. B* **84**, 115460 (2011).
59. Pereira, L. F. C. & Donadio, D. Divergence of the thermal conductivity in uniaxially strained graphene. *Phys. Rev. B* **87**, 125424 (2013).
60. Plimpton, S. J. Fast parallel algorithms for short-range molecular dynamics. *J. Comput. Phys.* **117**, 1 (1995).
61. Tersoff, J. Empirical interatomic potential for carbon, with applications to amorphous carbon. *Phys. Rev. Lett.* **61**, 2879 (1988).
62. Lindsay, L. & Broido, D. A. Optimized Tersoff and Brenner empirical potential parameters for lattice dynamics and phonon thermal transport in carbon nanotubes and graphene. *Phys. Rev. B* **81**, 205441 (2010).
63. Müller-Plathe, F. A simple nonequilibrium molecular dynamics method for calculating the thermal conductivity. *J. Chem. Phys.* **106**, 6082 (1997).

Acknowledgements

The authors would like to thank R.M. Tromer for a critical reading of the manuscript. I.M.F. and L.F.C.P. acknowledge financial support from the Brazilian Government Agency CAPES for the project “Physical properties of nanostructured materials” (Grant No. 3195/2014) via its Science Without Borders program, and the provision of computational resources by the High Performance Computing Center (NPAD) at UFRN.

Author Contributions

L.F.C.P. conceived the project. I.M.F. performed computer simulations under supervision of L.F.C.P. Both authors analyzed simulation results. L.F.C.P. wrote the first draft of the manuscript with input from I.M.F. Both authors contributed to the final version of the manuscript.

Additional Information

Competing Interests: The authors declare no competing interests.

Publisher's note: Springer Nature remains neutral with regard to jurisdictional claims in published maps and institutional affiliations.



Open Access This article is licensed under a Creative Commons Attribution 4.0 International License, which permits use, sharing, adaptation, distribution and reproduction in any medium or format, as long as you give appropriate credit to the original author(s) and the source, provide a link to the Creative Commons license, and indicate if changes were made. The images or other third party material in this article are included in the article's Creative Commons license, unless indicated otherwise in a credit line to the material. If material is not included in the article's Creative Commons license and your intended use is not permitted by statutory regulation or exceeds the permitted use, you will need to obtain permission directly from the copyright holder. To view a copy of this license, visit <http://creativecommons.org/licenses/by/4.0/>.

© The Author(s) 2018